

Defects in Ge and Si caused by 1 MeV Si⁺ implantation^{*}

D. P. Hickey^{a)}

Department of Materials Science and Engineering, University of Florida, 525 Engineering Building,
P.O. Box 116400, Gainesville, Florida 32611-6400

Z. L. Bryan,^{b)} K. S. Jones,^{c)} and R. G. Elliman^{d)}

Electronic Materials Engineering Department, Research School of Physical Sciences and Engineering,
The Australian National University, Canberra ACT 0200, Australia

E. E. Haller^{e)}

Materials Sciences Division, Lawrence Berkeley National Laboratory, 1 Cyclotron Road, Berkeley,
California 94720 and Department of Materials Science and Engineering, University of California at Berkeley,
Berkeley, California 94720

(Received 4 June 2007; accepted 19 December 2007; published 1 February 2008)

Cross-sectional transmission electron microscopy was used to study defect formation and evolution in the (001) Ge and Si wafers implanted with 1 MeV Si⁺ and 40 keV Si⁺ at a dose of $1 \times 10^{14} \text{ cm}^{-2}$. As expected, upon annealing, the {311} extended defects form and subsequently dissolve at the projected range for nonamorphizing implants into Si. However, in Ge, no {311} defect formation is observed for this nonamorphizing implant after annealing at temperatures between 350 and 850 °C. Instead, for the MeV implant, small dotlike defects are observed in Ge, which dissolve upon annealing between 650 and 750 °C for 10 min. © 2008 American Vacuum Society. [DOI: 10.1116/1.2834557]

I. INTRODUCTION

There is interest in replacing the channel material of transistors with germanium (Ge) instead of silicon (Si) because of its significantly higher carrier mobilities.¹ Recent advances in the use of high-*k* dielectrics have assisted in this regard by reducing the need for a stable Ge-based gate oxide. Additionally, SiGe alloys are being used in the current generation of devices to induce strain in the transistor channel to increase mobility.² Ion implantation remains the preferred method of introducing dopants into the extension region of transistors next to the gate, and is being used in current transistors.³ However, relatively little knowledge of the formation and evolution of ion-implantation related defects in Ge exists. Early studies of electron^{4,5} or light ion [hydrogen (H⁺) and helium (He⁺)]^{6–8} implants into Ge reported {311} defect formation. As recently as 2005, Akatsu *et al.* reported observing {311} defects in bulk Ge implanted with He⁺; however, the {311} defect has not been reported in Ge for any ion species heavier than He⁺. Recent studies of amorphizing implants into Ge have not reported any rodlike extended defects for low energy implants.⁹ To summarize, extended defects have been reported for light ion and electron irradiation but have not been seen for low energy implants using typical dopant atoms. It is well known that in Si, extended defect formation occurs for a wide range of implant and annealing conditions.¹⁰ Recent studies in SiGe alloys suggest that above 25% Ge, no {311} defects are observed, though only

alloys were studied.¹¹ Hence, the purpose of this study is to understand extended defect formation and evolution in bulk Ge after nonamorphizing Si⁺ implantation.

II. EXPERIMENT

Undoped (001) Czochralski-grown high-purity Ge wafers and undoped (001) Czochralski-grown Si wafers were Si⁺ implanted at 1 MeV and 40 keV with doses of $1 \times 10^{14} \text{ cm}^{-2}$. Samples were held at 30 °C during implantation and tilted 7° relative to the incident ions to avoid ion channeling. In Si, this implant regime is known to produce large, easily visible {311} extended defects after annealing.¹⁰ The 1 MeV Si⁺ implanted wafers were capped with 1000 Å of silicon dioxide (SiO₂) via plasma-enhanced chemical vapor deposition at 300 °C for 3 min to prevent possible oxidation during furnace annealing. Subsequent annealing was conducted in a Lindberg tube furnace for 10 min in a flowing nitrogen (N₂) environment at temperatures ranging from 350 to 850 °C for Ge, and from 650 to 950 °C for Si. This broad range of temperature for Ge encompasses those below the amorphous regrowth temperature of 400 °C (Ref. 12) and near the melting point of 938 °C.¹³ A FEI focused-ion beam (FIB) and *ex situ* lift-out system was used to prepare the Si and Ge cross-sectional transmission electron microscopy (XTEM) samples, while traditional polishing methods and etch chemistry appropriate to each material was used to prepare plan-view TEM (PTEM) samples.¹⁴ Transmission electron microscopy analysis was performed on a JEOL 200CX microscope using *g*₂₂₀ weak-beam dark-field (WBDF) imaging conditions and a JEOL 2010 using on-axis bright-field (BF) imaging conditions for high-resolution imaging.

^{*}No corrections received from author prior to publication.

^{a)}Tel.: 352-846-3038; electronic mail: dhickey@ufl.edu

^{b)}Electronic mail: zch513@ufl.edu

^{c)}Electronic mail: kjones@eng.ufl.edu

^{d)}Electronic mail: rob.elliman@anu.edu.au

^{e)}Electronic mail: eehaller@lbl.gov

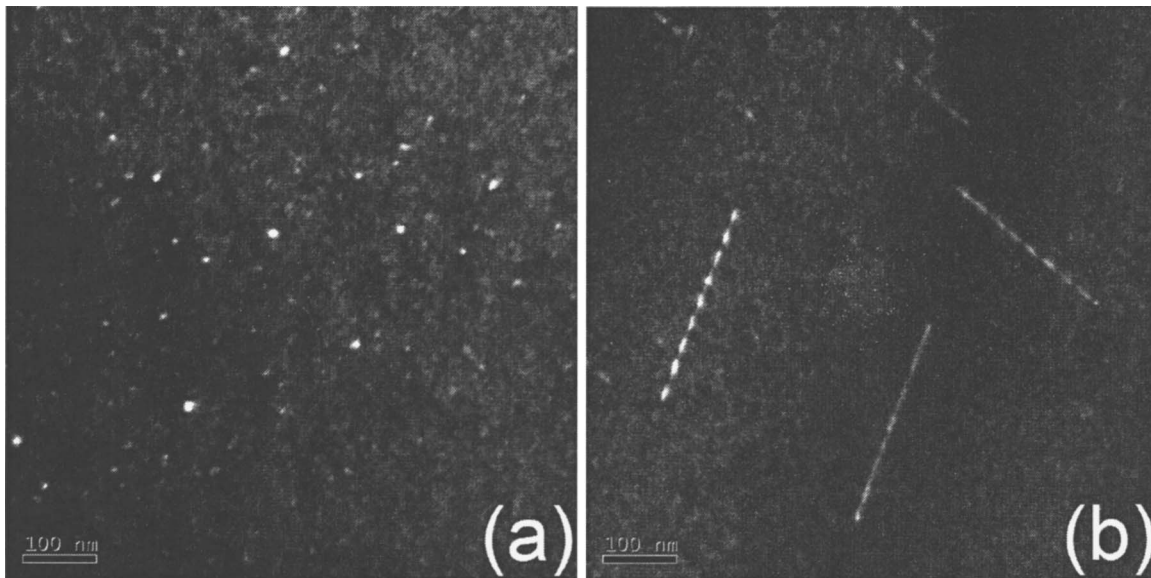


FIG. 1. WBDF XTEM images of (a) dotlike defects in Ge implanted with 1 MeV 1×10^{14} Si⁺ cm⁻² following annealing at 450 °C (50% $T_{MP, Ge}$) for 10 min and (b) {311} defects in Si with the same implantation following annealing at 850 °C (60% $T_{MP, Si}$) for 10 min.

III. RESULTS

Upon Si⁺ implantation at 1 MeV without annealing, WBDF XTEM imaging revealed small dotlike defects in the 1 MeV implanted Ge extending from the surface to 1.1 μm below the surface. In Si, however, no discernable defects were observed prior to annealing. Upon annealing, Ge defects and Si defects display radically different morphology, as seen on the same scale using WBDF PTEM imaging conditions. In Ge, defects appear as dotlike defects after annealing at 450 °C, which is 50% of the melting point (T_{MP}) for Ge, for 10 min as presented in Fig. 1(a). These defects are too small to produce a clear phase contrast image when imaged using high-resolution TEM conditions. The defects are an average size of approximately 12 nm in diameter over all annealing conditions. However, the defects in Si appear as rodlike defects, elongated along the $\langle 110 \rangle$ directions, and were at their coarsest after annealing for 10 min at 850 °C (60% $T_{MP, Si}$) as shown in Fig. 1(b). These rodlike defects are commonly referred to as {311} defects as these defects have {311}-type habit planes.¹¹

Microstructural evolution for the 1 MeV Si⁺ implantation into Ge and Si is shown in Fig. 2 on the same scale. The projected range (R_p) of the damage in Ge is predicted to be 0.91 μm below the surface, while the damage peak (R_D) should occur at 0.72 μm , according to simulations.¹⁵ This is in good agreement with TEM analysis, as the density of defects was greatest between R_D and R_p . The simulation also agrees with the experiment for the implant into Si, with a R_p and R_D of ~ 1.19 and 1.04 μm , respectively.

In Ge, the dotlike defects which appear immediately after implantation are shown after a 350 °C annealing for 10 min in Fig. 2(a). The defects decrease in density after the 450 and 550 °C annealing for 10 min, and remain until finally dissolving at temperatures between 650 and 750 °C, as shown in Figs. 2(b)–2(d). The defects decrease in density but their

average diameter remains at approximately 12 nm. However, in Si, after annealing for 10 min at 750 °C, extremely small rodlike defects begin to appear in densities right at the limit of detection, but are visible in the micrograph presented in Fig. 2(e). After 10 min at 800 °C, the defects have reduced in number but increased in size as shown in Fig. 2(f). This trend continues at 850 °C, where the defects have grown into large easily visible {311} extrinsic defects, averaging 170 nm in size with some as large as 300 nm, as evident by the micrograph in Fig. 2(g). Presented in Fig. 2(h), the defects have dissolved after 10 min at 950 °C.

For the lower energy (40 keV) implants, neither Si nor Ge show any defects after initial implantation using WBDF X- and P-TEM methods. Upon annealing, Si forms the characteristic {311} defects, visible both in XTEM and PTEM using WBDF diffraction conditions, as shown in Figs. 3(a) and 3(b), respectively. The majority of the defects lie in the region between R_D (approximately 36 nm) and R_p (approximately 68 nm), though some defects extend to the end of range of the implant, as observed in Fig. 3(a). In contrast, the Ge implanted with Si⁺ at 40 keV show no defects in WBDF XTEM for any annealing temperature. In PTEM, for some annealing temperatures (450 and 550 °C), dotlike defects are visible; however, the fact that defects are observed in the PTEM and not in the XTEM micrographs, coupled with the lack of defects at other anneal temperatures, may indicate that these dotlike defects seen in the Si⁺ implanted Ge samples at 40 keV are artifacts of the PTEM sample preparation process.

IV. DISCUSSION

Si defects have been well documented to follow a specific process. Theoretical submicroscopic interstitial clusters evolve into small {311} defects, and with increasing thermal budgets, larger defects grow at the expense of smaller

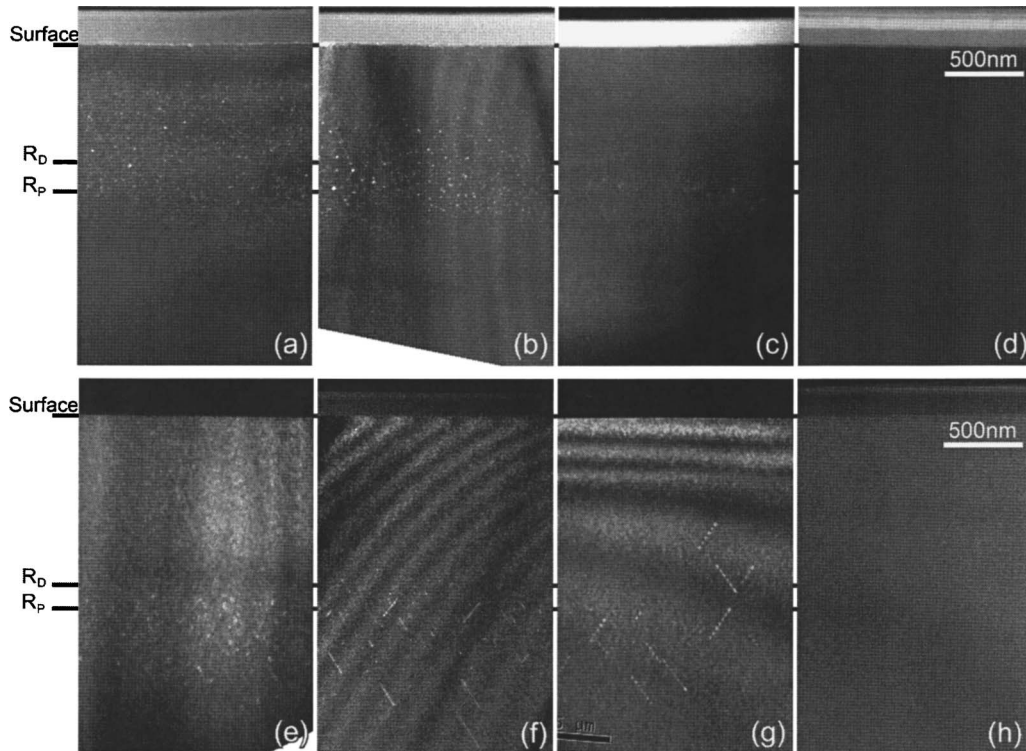


FIG. 2. WBDF XTEM images taken at g_{220} diffraction conditions of (001) oriented Ge implanted with 1 MeV 1×10^{14} Si⁺ cm⁻² for the following annealing conditions, 10 min at (a) 350 °C, (b) 450 °C, (c) 650 °C, (d) 750 °C, and of (001) oriented Si after 10 min at (e) 750 °C, (f) 800 °C, (g) 850 °C, and (h) 950 °C.

defects.¹⁰ In low Si⁺ implantation dose regimes, such as 1×10^{14} cm⁻², and with a high enough thermal budget, the large defects become unstable and dissolve.¹⁶ However, the evolution of the defect in Ge, under this same implant energy and dose regime, is quite different, as shown in Fig. 4. Though the density of the defects declines with annealing temperature [Fig. 4(a)], the size of the defects stays constant, in sharp contrast to the increasing size of the defects in Si [Fig. 4(b)].

A. Defect density analysis

Plan-view quantification of the Si⁺ implantation at 1 MeV is not possible because the defects are deeper than the Ge extinction distance for TEM analysis. However, defect count analysis is possible in the XTEM samples because these

samples were prepared using a standard automatic FIB process, so all samples are approximately the same thickness, about 100 nm. The density of defects can be derived from these XTEM images by the following method: each sample was made using the same automated XTEM procedure on a dual beam FEI focused-ion beam instrument, which resulted in samples uniformly thick, approximately 100 nm. Images of defects were then taken at various magnifications, always using the WBDF g_{220} imaging condition. Grids of $0.2 \times 0.2 \mu\text{m}^2$ were superimposed on the Ge images, from the surface to $1.5 \mu\text{m}$ below the surface, $0.4 \mu\text{m}$ past where defects were visible. Two different scientists independently counted the defects, and then the defect counts were averaged, with no significant discrepancy between the two scientists. The average between all data sample columns through

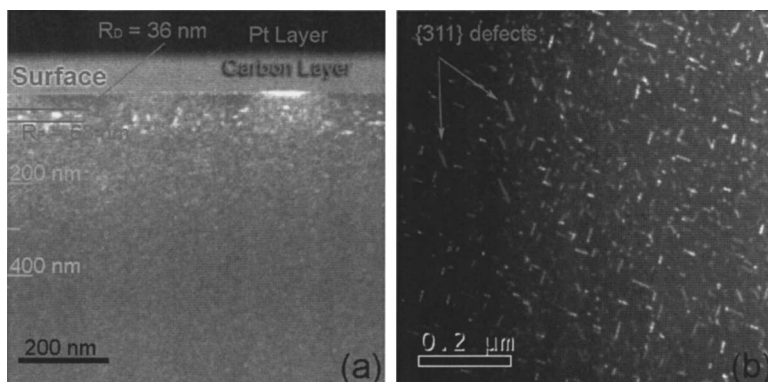


FIG. 3. WBDF images taken at g_{220} diffraction conditions of (001) oriented Si implanted with 40 keV 1×10^{14} Si⁺ cm⁻² annealed at 750 °C (53% $T_{MP\ Si}$) for 10 min: (a) XTEM and (b) PTEM.

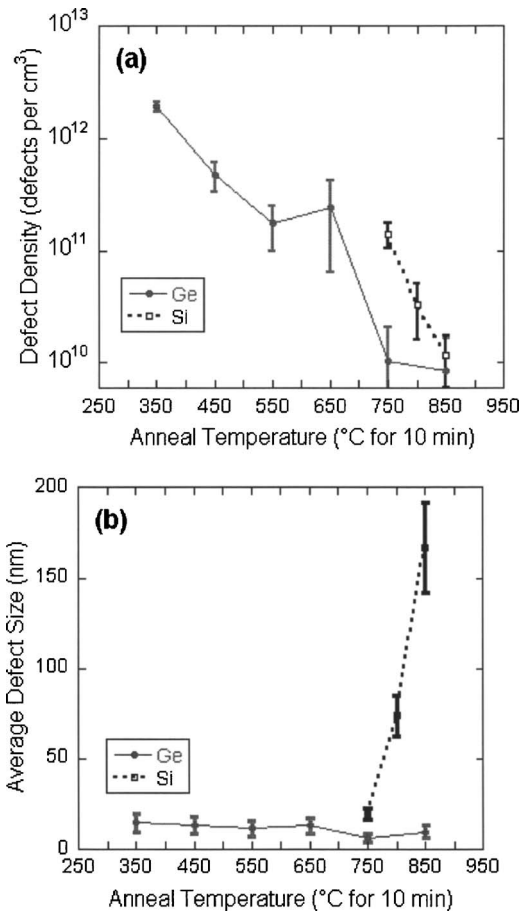


FIG. 4. Microstructure evolution of Ge and Si after annealing for 10 min at various temperatures: (a) defect density vs temperature and (b) average defect size vs temperature. The TEM detection limit in (a) is approximately 10^{10} cm^{-3} .

the material were converted to cm³ for plotting (for Ge, a column consisted of a $0.2 \times 0.1 \mu\text{m}^2$ area from the surface extending down into the sample, while for Si, a column consisted of $0.5 \times 0.1 \mu\text{m}^2$ to accommodate for the accurate counting of larger defects). Defect sizes were measured at two different magnifications. Using this method, the resolution limit for the detection of small defects (10 nm in diameter) is approximately $10^{10} \text{ defects/cm}^3$. Ge defect counts after annealing of 750 and 850 °C for 10 min are right at this detection limit, while Si defects after annealing of 650 and 950 °C were below this resolution (no defects were observed).

Using the above method, defect densities in both Ge and Si were determined. In Ge, after annealing at 350 °C for 10 min [Fig. 2(a)], $2 \times 10^{12} \text{ defects cm}^{-3}$ were observed. At 450 °C [Fig. 2(b)], the density of defects declined to approximately $5 \times 10^{11} \text{ defects cm}^{-3}$, and then leveled off at approximately $2 \times 10^{11} \text{ defects cm}^{-3}$ after annealing of 550 and 650 °C [Fig. 2(c)]. Defects in Ge dissolved completely at 750 °C [Fig. 2(d)] and 850 °C, and the defect counts in these images were right at the detection limit of this method. This is graphically represented in Fig. 4(a). Interestingly, the average size of the defect remains the same, approximately

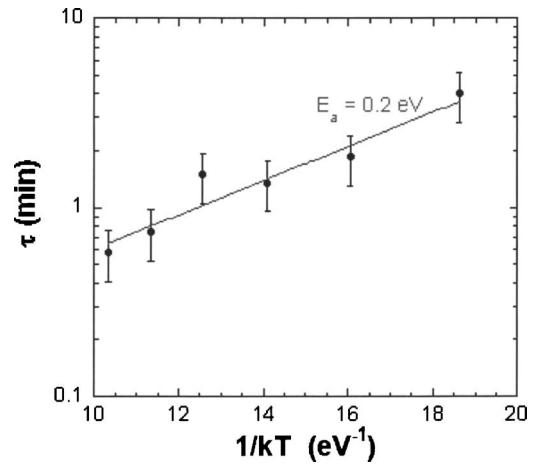


FIG. 5. Plot of the logarithm of τ vs $1/kT$ for 1 MeV Si⁺ implantation into Ge after 10 min of annealing. The value of E_a is approximately $0.2 \pm 0.1 \text{ eV}$.

10–15 nm [Fig. 4(b)] throughout the microstructural evolution. The Ge defects after 10 min at 450 °C may be small loops. However, either the small size or the off-axis habit plane prevented obvious identification using on-axis high-resolution phase contrast imaging. No {311} defects were observed in the high-resolution images.

B. Defect dissolution rate

Assuming an Arrhenius relationship between temperature and the dissolution rate of the Ge defects, an activation energy and time constant were derived. Beginning with the following two formulas, where D is the dissolution rate of the dotlike defects and is a function of time and temperature, D_0 is the number of defects at time zero, t is time, and τ is the time constant.

$$D(t, T) = D_0 e^{-t/\tau}. \quad (1)$$

τ is more explicitly defined as

$$\tau = \tau_0 e^{E_a/kT}, \quad (2)$$

where τ_0 is the time constant at time zero, E_a is the activation energy, k is Boltzmann's constant, and T is the temperature: From the defect analysis, the number of defects after implantation, but before annealing was approximately $1.18 \times 10^{12} \text{ cm}^{-2}$. However, this makes the activation energy calculation difficult, as the first value after annealing is $1.92 \times 10^{12} \text{ defects/cm}^2$, larger than the initial count. For the sake of calculation, D_0 is estimated to be slightly larger than the 350 °C quantity. Interesting, the increase, and then decrease, in visible defects between the as-implanted state and subsequent annealing may indicate that more than one mechanism is contributing to the defect evolution. Thus, τ at a given temperature may be estimated using Eq. (1). The value of E_a is obtained by plotting the logarithm of tau versus $1/kT$ and determining the slope, as presented in Fig. 5. Doing this, E_a is approximately $0.2 \pm 0.1 \text{ eV}$.

C. Defect location analysis

Defect location within each material differs between Ge and Si. In the 1 MeV Si⁺ implant into Ge, defects are seen immediately after implantation and stretch from the surface to the predicted R_p of approximately 0.91 μm . Defects in the same implant into Si are not seen until after annealing for 10 min at 750 °C, and are concentrated around and below the predicted R_p of $\sim 1.19 \mu\text{m}$. In Ge, the defect density peaks at depths shallower than the projected range, whereas in Si, the majority of defects resides below the projected range. Additionally, defects in Ge seem to dissolve more rapidly near the surface, whereas in Si, the ripening process of each defect is not affected by its proximity to the surface, as shown in Fig. 3. This phenomenon may be due to a difference in the stability of the vacancy population in the near-surface region of Ge versus Si.¹⁷ This hypothesis gains merit in light of a recent report that in SiGe, MeV implants into 30 at. % Ge concentration SiGe alloys showed near-surface vacancy nanocavities, confirmed by positron analysis.¹⁸ Crosby *et al.* also noted differences in defect formation for increasing concentrations in SiGe alloys. The experiment used SiGe, with 0, 2, 5, 25, 35, and 50 at. % Ge, with Si⁺ implantation at 40 keV, with a dose of 1×10^{14} Si⁺/cm² and annealed at 750 °C for various times. They noted the {311} defect formation, similar to Fig. 4(b) for low concentrations of Ge. At 25% Ge and subsequent higher concentrations, no {311} defects were observed, but instead, dislocation loops formed immediately. No XTEM analyses were reported in the previous study to compare to the current results. The results of this study agree with the presented trend of Crosby *et al.* as no {311} defects were visible in 40 keV Si⁺ implanted pure Ge. Future work focusing on the defect formation in lower energy implants into pure Ge is necessary to confirm the lack of defects shown in this study.

Ge does not display the characteristic behavior of Si for nonamorphizing implants. Although the {311} defects were reported for H⁺ implantation in Ge (Ref. 7) and for other electron or light ion implants,^{4,6} no {311} defects, platelets, or any type of planar defects were observed for heavier ion implants. This is consistent with the observations of Crosby *et al.* of decreasing density of {311} defects in SiGe alloys with increasing Ge content.¹¹ Crosby *et al.* suggested that the bond strength¹³ differences between Si and Ge may cause the {311} defect to become thermodynamically unfavorable at high Ge content. Unlike Si, the location of the defects in Ge is closer to the surface implying some of the defects may be intrinsic. In addition, the size distribution of the defects in Ge remains relatively constant throughout the annealing process. These results suggest that the {311} defect formation may be unique to Si.

V. CONCLUSION

Cross-sectional TEM was used to study the defect formation and evolution after Si⁺ implants in the (001) Ge and Si wafers. As expected, upon annealing, the {311} extended defects form and subsequently dissolve at the projected range for nonamorphizing implants into Si. In Ge, no {311} defect formation is observed for this nonamorphizing implant after annealing at temperatures between 350 and 850 °C. Instead, for the high energy (1 MeV) implant, small dotlike defects are observed in Ge, which dissolve upon annealing between 650 and 750 °C for 10 min. No defects are observed for the lower energy (40 keV) implant in Ge.

ACKNOWLEDGMENTS

The authors would like to acknowledge the Major Analytical Instrumentation Center at the University of Florida. This work was supported by the Semiconductor Research Corporation under Contract No. 00057787.

- ¹L. L. Berger, in *CRC Handbook of Chemistry and Physics*, edited by David R. Lide (Taylor & Francis Group, London, 2005), pp. 12–82.
- ²S. E. Thompson *et al.*, IEEE Trans. Electron Devices **51**, 1790 (2004).
- ³P. R. Chidambaram, C. Bowen, S. Chakravarthi, C. Machala, and R. Wise, IEEE Trans. Electron Devices **53**, 944 (2006).
- ⁴C. A. Ferreira Lima and A. Howie, Philos. Mag. **34**, 1054 (1976).
- ⁵H. Bartsch, D. Hoehl, and G. Kastner, Phys. Status Solidi A **83**, 543 (1984); S. Furuno, K. Izui, and H. Otsu, Jpn. J. Appl. Phys. **15**, 889 (1976).
- ⁶L. Hutchison, A. L. Aseev, and L. I. Fedina, Microscopy of Semiconducting Materials 1993 (unpublished), pp. 41–46.
- ⁷T. Akatsu, K. K. Bourdelle, C. Richtarch, B. Faure, and F. Letertre, Appl. Phys. Lett. **86**, 181910 (2005).
- ⁸A. L. Aseev, V. M. Ivakhnishin, V. F. Stas', and L. S. Smirnov, Sov. Phys. Solid State [translation of Fiz. Tverd. Tela (Leningrad)] **25**, 1786 (1983).
- ⁹A. Satta, E. Simoen, R. Duffy, T. Janssens, T. Clarysse, A. Benedetti, M. Meuris, and W. Vandervorst, Appl. Phys. Lett. **88**, 162118 (2006); A. Satta *et al.*, J. Electrochem. Soc. **153**, G229 (2006); A. Satta *et al.*, J. Vac. Sci. Technol. B **24**, 494 (2006); T. Janssens, C. Huyghebaert, D. Vanhaeren, G. Winderickx, A. Satta, M. Meuris, and W. Vandervorst, J. Vac. Sci. Technol. B **24**, 510 (2006); A. Satta, E. Simoen, T. Clarysse, T. Janssens, A. Benedetti, B. De Jaeger, M. Meuris, and W. Vandervorst, Appl. Phys. Lett. **87**, 172109 (2005).
- ¹⁰K. S. Jones, S. Prussin, and E. R. Weber, Appl. Phys. A: Mater. Sci. Process. **45**, 1 (1988).
- ¹¹R. Crosby, K. S. Jones, M. E. Law, A. N. Larsen, and J. L. Hansen, J. Vac. Sci. Technol. B **22**, 468 (2004).
- ¹²L. Csepregi, R. P. Kullen, J. W. Mayer, and T. W. Sigmon, Solid State Commun. **21**, 1019 (1977); K. Zellama, J. F. Morhange, P. Germain, and J. C. Bourgoin, Phys. Status Solidi A **56**, 717 (1979).
- ¹³in *CRC Handbook of Chemistry and Physics*, edited by David R. Lide (Taylor & Francis, London, 2005), pp. 4–125.
- ¹⁴K. C. Thompson-Russell and J. W. Edington, in *Monographs in Practical Electron Microscopy in Materials Science*, edited by J. W. Edington (Philips Technical Library, Holland, 1977), Vol. 5, p. 62.
- ¹⁵J. F. Ziegler, Nucl. Instrum. Methods Phys. Res. B **219–20**, 1027 (2004).
- ¹⁶D. J. Eaglesham, P. A. Stolk, H.-J. Gossmann, and J. M. Poate, Appl. Phys. Lett. **65**, 2305 (1994).
- ¹⁷V. C. Venezia, T. E. Haynes, A. Agarwal, L. Pelaz, H. J. Gossmann, D. C. Jacobson, and D. J. Eaglesham, Appl. Phys. Lett. **74**, 1299 (1999).
- ¹⁸R. Kogler, A. Mucklich, W. Skorupa, A. Peeva, A. Y. Kuznetsov, J. S. Christensen, and B. G. Svensson, J. Appl. Phys. **101**, 033508 (2007).